Reclaiming Motor Functions after Complete Spinal Cord Injury using Epidural Minimally Invasive Brain-Computer Interface

Dingkun Liu[1#], Yongzhi Shan[2#], Penghu Wei[2#], Wenzheng Li[1], Honglai Xu[3], Fangshuo Liang[1], Tao Liu[3], Guoguang Zhao[2*], Bo Hong[1*]

[1]Department of Biomedical Engineering, School of Medicine, Tsinghua University, Beijing, China.
[2]Department of Neurosurgery, Xuanwu Hospital of Capital Medical University, National Medical Center for Neurological Diseases, Beijing, China.
[3]Neuracle Technology Co., Shanghai, China.

[#] Equal contribution
* Corresponding author

E-mail: hongbo@tsinghua.edu.cn

Abstract: Spinal cord injuries significantly impair patients' ability to perform daily activities independently. While invasive brain-computer interfaces (BCIs) offer high communication bandwidth to assist and rehabilitate these patients, their invasiveness limits broader adoption. We developed a minimally invasive BCI system that balances safety and communication bandwidth to restore hand functions. This system enables real-time, precise control of hand movements and effective hand function rehabilitation, requiring less than 10 minutes of calibration time and maintaining an average grasping detection F1-score of 0.91 over a 9-month period of home use. A tetraplegia patient caused by complete spinal cord injury was recruited in this study. With the assistance of the brain-computer interface, the patient can successfully perform object grasping and daily tasks involving hand functions, achieving a 100% success rate in an object transfer test. Additionally, the patient showed substantial neurological recovery through consecutive BCI upper limb training, regaining the ability to hold objects without BCI assistance. The patient demonstrated a 5-point improvement in ISNCSCI upper limb motor scores and a 27-point increase in the Action Research Arm Test (ARAT). Improvements in electrophysiological assessments point to a considerable recovery in impaired neural circuits. The cerebral-spinal channels established via this BCI system offer a promising new approach for treating spinal cord injuries and restoring hand functions.

Keywords: Minimally Invasive Brain-Computer Interface; Motor Imagery; Sensory Evoked Potentials; Functional Magnetic Resonance Imaging; Riemannian Geometry.

Introduction

Spinal cord injuries (SCI) can lead to permanent paralysis of the limbs, especially when the injury occurs in the cervical region, resulting in the loss of motor function in all four limbs. Implantable brain-computer interfaces (BCIs) present a novel solution to help patients regain some motor functions[1,2]. Combined with epidural spinal cord stimulation systems, these interfaces can facilitate functional rehabilitation[3,4]. Current research on implantable BCIs primarily focuses on increasing their communication bandwidth. However, the long-term efficacy and reliability of these systems are often constrained by safety concerns[5,6]. Few studies have investigated how to enhance the safety of implantable BCIs to achieve an optimal balance between communication bandwidth and safety. Additionally, BCIs combined with epidural spinal cord stimulation have been shown to enhance axonal excitability, induce closed-loop electrical activity, and promote active rehabilitation of the brain-spinal cord pathways. This combination can potentially restore voluntary walking abilities in patients[3,7]. However, it remains unclear whether the brain-spinal cord pathways can autonomously recover through BCI-induced sensory and motor feedback without external electrical stimulation.

In our previous research, we designed and validated a brain-computer interface (BCI) system called NEO (Neural Electrical Opportunity) using epidural electrodes and bidirectional wireless communication in animal models. The NEO system ensures long-term safety and effectiveness through its battery-free, bidirectional design and epidural electrodes that keep the brain tissue intact.

In this study, we utilized the NEO system to develop a long-term hand movement assistance system for a patient with complete C4 spinal cord injury resulting in quadriplegia. We investigated whether neural rehabilitation could be achieved through the coupling of cortical descending control signals and ascending sensory signals at the injury site, without relying on external electrical stimulation.

The Epidural Minimally Invasive BCI

To create a balanced bridge between bandwidth and safety in brain-upper limb control, we designed an epidural wireless minimally invasive brain-computer interface (BCI) system, named NEO.

The implantable part of the NEO system consists of a titanium alloy implant, a coil, and two electrode adaptors extending outward. The entire system is sealed with silicone material (Fig. 1b). The epidural electrodes are connected to the implant via the electrode adaptor, with each electrode featuring four bidirectional contacts capable of both recording and stimulating. These electrodes have a diameter of 3.2 mm and a center-to-center distance of 8 mm. The system operates at a sampling rate of 1 kHz. It includes two sets of coils: the first set supplies power through near-field coupling, and the second set transmits collected neural signals via Bluetooth.

This design has two main characteristics. First, it employs minimally invasive epidural electrodes. These electrodes, placed on the dura mater, without penetrating the dura, preventing a strong immune response and ensuring long-term effectiveness. Second, the system utilizes bidirectional wireless communication for both power and information transmission (Fig. 1c). Wireless communication reduces the risk of infection by eliminating the need for open wounds. The implant does not contain a battery; instead, it is powered wirelessly via the coils, which also handle bidirectional data transmission. This battery-free design ensures that the device's lifespan is not limited by battery life. While a similar design has been widely adopted in cochlear implants[8], it has not yet been reported in the field of implanted brain-computer interfaces.

Signals are received by a relay attached to the arm and transmitted to a computer via Bluetooth or WIFI. The computer decodes the patient's motor control signals continuously from the neural data and drives an external pneumatic glove (Fubo Co.) (Fig. 1a, Extended Data Video 1). When the patient imagines grasping and holding, the pneumatic glove grasps; when the patient imagines relaxing, the glove extends.

Precise Implantation of Minimally Invasive BCI

This study is part of a clinical trial for the implantable closed-loop BCI system (NEO) (clinicaltrials.gov, NCT05920174), which was approved by the Xuanwu Hospital Ethics Committee in April 2023. We recruited a patient who suffered a spinal cord injury in a car accident more than 10 years before, resulting in limited hand motor function, making grasping, holding, and pinching actions impossible (Extended Data Video 2). Prior to NEO implantation, the patient underwent a neurological assessment and was diagnosed with complete C4 spinal cord injury (AIS-A, Extended Data Table 1, Extended Data Fig. 1).

To obtain the most informative neural signals related to hand grasping with a minimal number of electrodes, we performed preoperative planning for the BCI electrode implantation using functional MRI (fMRI). Research indicates that the transmission of ascending signals is crucial for SCI rehabilitation[9]. Therefore, our paradigm included fMRI imaging of both active and passive grasping attempts. The active grasping paradigm requires the subject to perform motor imagery based on cues, whereas the passive grasping paradigm requires the subject to perceive the sensation of the experimenter assisting him in grasping and releasing. The active grasping paradigm localized the sensory-motor area responsible for the patient's hand, while the passive grasping paradigm assessed the transmission of ascending sensory signals (Extended Data Fig. 2). Additionally, we collected CT and structural MRI images of the patient to determine the implantation site.

The significant activation regions were projected from the fMRI onto a 3D model of the cortex, using 3D modeling software to simulate electrode placement (Extended Data Fig. 2). The position of the implant was determined using skull structure obtained from CT images, selecting an area with suitable thickness. The final plan was then output to a surgical navigation system to guide the implantation procedure.

The minimally invasive BCI implantation surgery was completed in October 2023. Conducted under general anesthesia, a coronal incision was made on the left scalp to place the internal device, coil, and electrode pads. Following the preoperative plan, a circular window was created in the skull, exposing the dura mater, and the electrodes were sutured onto the dura mater according to the planned positions. The bone flap was then repositioned and secured. A 3-4 mm deep groove was created on the skull surface to embed the implant, which was fixed using bone screws, and the incision was sutured closed. The patient was discharged within 24 hours after all clinical observations were completed.

Postoperatively, we extracted the electrode positions from the patient's postoperative CT images and registered them to the preoperative MRI images, obtaining a map of the eight electrode positions. The first four electrodes were placed above the precentral gyrus, while the latter four were above the postcentral gyrus. Electrodes 2-3 in the precentral gyrus and electrodes 7-8 in the postcentral gyrus covered the most prominent activated hand areas identified by fMRI during hand movement imagination (Fig. 1d, Extended Data Fig. 2).

Long-term Characteristics of Epidural Signals

Generally, brain electrophysiological recordings can be divided into three distinct levels: scalp electroencephalography (EEG), subdural electrocorticography (sECoG), and action potential recordings. These methods vary in safety and signal quality, with EEG being the safest but having the lowest signal quality, and action potential recordings being the least safe but offering the highest signal quality. We propose that epidural electrocorticography (eECoG) represents a fourth type, which theoretically provides higher safety than sECoG[6] and is considered minimally invasive. Its spatio-temporal-spectral characteristics are distinct from the other three methods. Currently, there is limited information on long-term eECoG recordings, and we have obtained substantial minimally invasive eECoG signals for the first time. By analyzing these signals' spatio-temporal-spectral characteristics, we can guide the design of decoding methods for epidural minimally invasive BCIs.

Fig. 1e shows the average event-related spectrum perturbation (ERSP) pattern of 1700 trials of imagined hand grasping versus rest by the patient. The spectrum pattern exhibits a typical dual-frequency feature, including low-frequency (15-50 Hz) event-related desynchronization (ERD) and high-frequency (>50 Hz) event-related synchronization (ERS).

We compared the spatio-temporal-spectral characteristics of the patient's eECoG with subdural ECoG datasets[10], the patient's scalp EEG, and a published EEG dataset[11]. Scalp EEG showed no significant ERSP from the low gamma (>40 Hz) frequency band onwards ($p=0.42$, Fig. 2a). Both eECoG and sECoG exhibited low-frequency ERD and high-frequency ERS effects. It is particularly noteworthy that the frequency upper limit of eECoG can exceed 200 Hz, which is significantly higher than that of scalp EEG (Fig. 2a). The power spectral density of eECoG was lower than that of sECoG in different frequency bands but higher than that of scalp EEG in the high-frequency range (20-75 Hz) (Fig. 2b). Spatially, by comparing the relationship between channel correlation and electrode distance, we qualitatively verified the spatial resolution

differences among different levels of brain electrophysiological recordings. The correlation between EEG channels decreased slowly with increasing electrode distance, indicating lower spatial resolution. The correlation between sECoG channels decreased most rapidly with increasing electrode distance, indicating the highest spatial resolution, with eECoG showing moderate spatial resolution (Fig. 2c).

The quality of long-term eECoG signals improved continuously with training. Spatially, electrode 8 showed the strongest high gamma (HG) response during imagined hand movement, and all electrodes' HG responses significantly increased over nine months of training ($p<0.001$, Fig. 2d). The ERSP effects of electrodes in both the precentral and postcentral gyrus during imagined hand movement also continuously enhanced with training (Fig. 2e-f). Additionally, the HG energy during resting and movement states significantly increased with time ($p<0.001$, Fig. 2h). We continuously measured the impedance changes to reflect alterations in the patient's intracranial environment post-surgery. The results showed only a slight increase in electrode impedance (<600 Ω), which gradually stabilized (Fig. 2g).

BCI-assisted Continuous Natural Grasping

In our previous analysis, we confirmed the wideband characteristics of minimally invasive eECoG, which provides spatial resolution between sECoG and EEG. We also observed that the signal amplitude improves with continuous training. To accurately decode the patient's natural grasping movements and achieve motor assistance with the BCI, our decoder design needs to integrate multi-band frequency information, restore source space activity, and maintain invariance to signal amplitude over long periods.

Firstly, eECoG features were extracted by combining spatial and spectral information into a covariance matrix, utilizing scale-invariant Riemannian metrics for classification to address long-term distribution shift in neural features[12] (see Methods: Spatio-Spectral Riemannian Geometry Decoding Method). Secondly, a hidden Markov model (HMM) was employed to manage the temporal dependencies of continuous grasping actions, ensuring prediction accuracy and stability (Extended Data Fig. 3 and 4). This approach was compared with two commonly used BCI decoding methods: a linear method[1], which uses linear spatio-temporal-spectral features, and the Common Spatial Pattern (CSP) method[13], which uses multi-band spatial patterns (see Methods: The Control Decoding Methods). Both methods are widely used in BCI applications.

The BCI calibration was completed within 10 minutes using a block design paradigm alternating between imagined grasping and resting. For the BCI testing and rehabilitation training task, the patient was instructed to use motor imagery to control a pneumatic hand to move an object from the center of a 3x3 grid to one of the eight surrounding cells (Fig. 3a, Extended Data Fig. 5). After 10 minutes of calibration, the patient achieved a decoding accuracy of 94% (Chance level: 77%) and a grasp event detection F1 score of 0.8 (Chance level: 0.09). Despite the continuous increase in the patient's high-frequency amplitude, indicating improving signal quality, this amplitude change affects the classification accuracy of linear decoders but has minimal impact on

the AIRM[12]. Over nine months, the patient's grasp event F1 score steadily increased, surpassing 0.9 after three months. The long-term stability of the Riemannian method was superior to both Linear and CSP methods, with the F1 score consistently improving and feature distribution shifts being less pronounced (Fig. 3i, Extended Data Fig. 6), and an average latency of 1.23±0.33s. In the 3x3 grid test, the success rate was 100% within 10 seconds with BCI assistance, compared to 35% without it (Fig. 3b-d, 181-185 days after implantation, Extended Data Video 3). The model's consistent and accurate predictions during the autonomous grasping sessions demonstrate the effectiveness of the BCI system. With BCI assistance, the grasping time was evenly distributed between the start and end points, while without assistance, it was concentrated at the start point, indicating improved grasping efficiency with BCI assistance (Fig. 3e-f, h). We compared the performance of our system using EEG collected from the subject. The grasp event F1 score for the EEG-based decoder was only 0.16±0.11 (s.d.) (Chance level: 0.07), while for the eECoG it was 0.90±0.06 (s.d.) (Chance level: 0.09) (Fig. 3g).

In a home setting, the BCI can assist with various tasks requiring grasping. However, activities like eating and drinking generate significant electromyographic (EMG) noise, which interferes with the decoder. Since the spatial distribution of EMG noise differs from that of grasping movements, the Riemannian geometry method, which is highly sensitive to spatial patterns, can filter out noise without supervised training (Extended Data Fig. 7). Compared to the Riemannian geometry method, the Linear and CSP methods had a false activation rate (FAR) of 100% during chewing, while the Riemannian geometry method had a FAR of only 20% (Fig. 3j). Using the Riemannian geometry decoding method, the patient could perform grasp-related tasks such as eating and drinking with BCI assistance (Extended Data Video 4, 267 days after implantation).

Hand Function Rehabilitation and Electrophysiology Assessment

The regeneration of spinal connections induced by neuroplasticity from electrical activity has been demonstrated in relevant literature[3,14,15]. In this study, electrical activity was generated by descending signals actively sent from the brain and ascending signals from muscle sensory feedback. This process is more natural and aligns better with the patient's physiological patterns compared to direct electrical stimulation. Indeed, during nine months of continuous training, significant neurophysiological and functional recovery was observed in the patient.

Somatosensory Evoked Potentials (SEPs) are used to assess sensory information conduction. SEPs are elicited by electrically stimulating peripheral nerves and recording the resulting electrical activity as it travels through the sensory pathways to the corresponding areas of the brain, such as the precentral and postcentral gyri. Thus, SEPs reflect the transmission of sensory information from peripheral receptors through the spinal cord to the brain, making them a useful tool for evaluating the extent of spinal cord injury and the progress of recovery[16,17]. SEP testing involves stimulating the median, radial, and ulnar nerves of the patient's right arm (corresponding to C6-T1, C5-C8, and C8-T1, respectively) with a constant current and recording the SEPs from the precentral and postcentral gyri using the NEO epidural electrodes (Fig. 4a). Changes in SEP signals from the radial, median, and ulnar nerves correspond to the recovery status of the sensory pathways at different levels of the spinal cord. The strongest and most stable SEP responses were

observed in channel 5 (Fig. 4b, Extended Data Fig. 8). The radial nerve corresponds to spinal segments above the injury level, the median nerve is near the injury level, and the ulnar nerve is below it. Consequently, it is expected that SEPs from the radial nerve will not show significant growth during recovery, while SEPs from the median nerve will show some improvement, and SEPs from the ulnar nerve might show less improvement. Over 9 months, the amplitude of SEPs elicited by median nerve stimulation in channel 5 increased significantly, whereas the radial nerve did not show significant changes (Fig. 4c). Comparing the first and nineth months, the mean amplitude of early (15-35ms) and late (40-80ms) components of median nerve SEPs increased significantly across most channels. The late component of ulnar nerve SEPs increased significantly in most channels, but the early component did not show a significant increase. The radial nerve showed no significant increase for either component in all channels but channel 4, which showed a significant increase for late component (Fig. 4d-e, bootstrap permutation test, fdr corrected, statistical p-values in Extended Data Table 2).

The patient's neurological scale assessments and hand function evaluations corresponded with the SEP changes. However, due to the patient's use of Baclofen and Pregabalin in the sixth month, there was a notable decrease in sensory and motor scores. The patient's upper limb motor score on the International Standards for Neurological Classification of Spinal Cord Injury (ISNCSCI) scale increased by 5 points over nine months, with changes concentrated in the C5-C8 segments, and the motor level dropping from C5 to C6. The sensory score increased by 8 points, peaking at 11 points in the fifth month, mostly in the C5-T4 segments (Fig. 4f-g, Extended Data Table 1). The Action Research Arm Test (ARAT) scale[18], which evaluates hand functions, including grasp, grip, pinch and gross movements, showed a 16-point improvement in the patient's right hand and a 11-point improvement in the left hand after nine months. The main improvement was in the grasp score, with the trained right hand showing more improvement than the left hand (Fig. 4i, Extended Data Table 3). For example, in the ARAT grasp test, the patient was able to grasp a 5 cm wooden block faster in the fifth month compared to the third month (3.9 s vs. 6.1 s) and was also able to successfully grasp a 7.5 cm wooden block in the fifth month (Fig. 4h, j-k). The patient completed the ARAT grasping part test before the surgery. Compared to the preoperative results, the grasping speed and success rate for 2.5 cm and 5 cm wooden blocks were significantly improved five months after the surgery (Extended Data Video 2).

Discussion

This study presents the first human trial of a bidirectional, wireless, and minimally invasive epidural BCI system. We developed a novel brain-spine rehabilitation pathway entirely based on the patient’s autonomous neural activities. This pathway enabled a patient with a complete C4 spinal cord injury to regain voluntary hand grasping ability. Furthermore, active rehabilitation training using the BCI facilitated a stable recovery of this autonomous grasping function. Significant and consistent improvements were observed in neurological scales, hand function assessments, and electrophysiological tests.

Implantable brain-computer interfaces often face a trade-off between communication bandwidth and safety. Typically, a higher channel number leads to higher bandwidth but lower safety. The

wireless, minimally invasive epidural BCI system developed in this study, featuring wireless power and transmission with a battery-free, closed-wound design, ensures long-term safety and stability for home use while effectively facilitating hand function restoration and rehabilitation. Although BCIs based on microelectrode implants can achieve similar functions, their long-term stability is limited by issues such as electrode displacement and glial cell encapsulation, necessitating frequent recalibration. Some BCIs using subdural cortical electrodes have been reported to maintain high long-term stability, requiring no recalibration for 2-6 months[19,20]. However, subdural electrodes pose a higher risk of adverse effects such as hematomas, intracranial hemorrhage, brain infarction, and cerebral edema due to direct pressure on brain tissue[6,21]. In contrast, minimally invasive epidural brain-computer interfaces offer significant advantages in long-term stability. The electrodes are placed outside the dura mater, providing structural support without damaging or compressing brain tissue. Consequently, the minimally invasive epidural electrodes exhibit better long-term stability, with signal quality improving over a nine-month period. Additionally, decoding performance remains stable over nine months with only 10 minutes of calibration.

In this study, we demonstrated for the first time that a minimally invasive BCI system, relying solely on the patient's autonomous sensory ascending and motor descending signals, can induce spinal circuit reconstruction, leading to the rehabilitation of upper limb sensory and motor functions in a patient with complete spinal cord injury. Previous studies have validated the effectiveness of brain-controlled spinal cord injury rehabilitation systems based on this principle[3,22,23], but they largely depend on electrical stimulation of limbs[23] or the spinal cord[3] to induce recovery. Our research confirmed the feasibility of directly using the body's own ascending and descending signals to facilitate upper limb rehabilitation. Additionally, there is a hypothesis that electrical stimulation of the spinal cord enhances the excitability of afferent nerves, thereby inducing neural circuit remodeling[7,15]. This method complements our approach and could be combined in the future to improve brain-controlled upper limb rehabilitation outcomes.

Our study also established a quantitative assessment method for neural function rehabilitation based on SEP (somatosensory evoked potential) using NEO system. The trend of changes in the amplitude of different SEP components was highly consistent with the patient's rehabilitation progress. At the sixth month, the patient was taking Baclofen and Pregabalin, both of which have inhibitory effects on the central nervous system. These medications exert global suppression on the central system, while SEP, as a primary cortical response to sensory information, is theoretically less affected by such medications compared to higher-level brain activities involved in subjective sensory perception. The results showed that SEP test outcomes were less disturbed than the sensory scores on the ISNCSCI scale, more accurately reflecting the connectivity of spinal neural circuits. Given that similar medications are commonly used by SCI patients, the stability of SEP provides a better assessment of the patient's sensory perception.

This study is a prospective investigation of a novel brain-computer interface, reporting results from a single subject. Consequently, the rehabilitation effects for patients with different injury locations or severities remain uncertain. However, our approach theoretically holds potential for application to other spinal cord injury patients. Firstly, the case we reported is an AIS-A level case, representing the most severe level of spinal cord injury. Patients with less severe injuries

would have more residual connections, providing better conditions for rehabilitation. Secondly, our system is highly reliable, with high decoding accuracy and long-term stability, making it highly scalable. Similar patients can quickly calibrate and use the system at home for long-term, effective rehabilitation training.

Methods

Clinical Protocol and Subject

This study was approved by the ethics committee of Xuanwu Hospital in April 2023 and registered for international and domestic clinical trials of implanted medical devices (NCT05920174) to conduct research on the implanted closed-loop brain-computer interface system (NEO). The surgery was performed at Xuanwu Hospital, with other related studies conducted at Tsinghua University and the patient's home. Our study includes three main phases: preoperative functional screening, surgery, a one-month calibration and adjustment period, and an eight-month BCI assisted active rehabilitation training period. The rehabilitation training involved a total of 100 sessions, each lasting 1-3 hours, personalized according to the patient's progress. In the 9^{th} month, the training load was doubled to maximize the patient's recovery outcomes.

The participant is a male who sustained a spinal cord injury more than 10 years ago due to a car accident. The participant signed a written informed consent before participation. Moreover, the participant gave his consent for the material depicting himself to appear in the contribution and to be published in the journal and associated works without limit on the duration of publication, in any form or medium.

Before the surgery, the patient underwent a neurological impairment assessment, currently diagnosed as a complete C4 spinal cord injury (ASIA-A, Extended Data Table 1). The patient's muscle tone was rated at level 2-3 on the Modified Ashworth Scale (MAS), indicating an increase in muscle tone that affects passive movement within the range of motion. The patient reported taking Baclofen (10mg/day) and Pregabalin (75mg/day) to relieve spasms at the sixth month post-surgery. This symptom has persisted since the injury and is unrelated to the BCI implant.

Functional MRI Localization

Before the implantation surgery, the subject underwent a head MRI on a 3.0T scanner (Siemens, Prisma) to locate brain areas associated with hand sensory and motor functions. Functional MRI (fMRI) was acquired using a gradient echo planar imaging (EPI) sequence with the following parameters: matrix size 100×100, resolution 2×2×2 mm^3, repetition time (TR) 2 s, echo time (TE) 30 ms. The scan covered the entire brain with 72 slices. T1-weighted MRI structural images were acquired using a magnetization-prepared rapid gradient-echo (MPRAGE) sequence with parameters: matrix size 256×256, resolution 1×1×1 mm^3, and 208 slices.

The fMRI paradigm was used to locate the subject's sensorimotor areas related to hand movement. The paradigm consisted of two parts. The first part involved passive movement, where two experimenters assisted the subject with passive fist clenching on the left and right sides at a

frequency of approximately 0.5 Hz. This was designed to test whether sensory information could be transmitted to the cortex, indicating the condition of the subject's ascending pathways. The second part involved motor imagery, where the subject was asked to imagine moving their left or right hand in a familiar manner. This was used to locate the hand motor areas in the primary motor (M1) and primary sensory (S1) cortices. The block design included two alternating conditions: movement and rest. At the beginning of the movement condition, an arrow pointing left or right appeared on the screen with a text prompt to "start imagining left hand/right hand movement." At the beginning of the rest condition, an image of a teacup appeared with a text prompt to "rest, relax, stay calm," instructing the subject to remain relaxed during this period. Each condition lasted 14 seconds (7 TRs, yielding 7 fMRI frames), repeated for 14 cycles. The left- and right-hand conditions alternated with a rest condition in between (Extended Data Fig. 2).

Surgical Planning

Based on the results of the functional MRI activations, we developed a surgical implantation plan for the subject. Using the fMRI activation heatmaps combined with anatomical localization of the hand motor and sensory areas, we performed 3D modeling to select specific sites on the precentral and postcentral gyri for the right hand, where epidural cortical electrodes were placed to cover regions of significant fMRI activation (Extended Data Fig. 2). The internal device was implanted into the flat skull behind the ear, ensuring sufficient bone thickness, avoiding the temporalis muscle, and facilitating wireless charging.

To effectively integrate the electrode positioning from the surgical plan with the surgical navigation system, a novel engineering method was developed to address compatibility issues between the 3D model and the navigation system. The cortex was segmented using FreeSurfer, and an individualized cortical model of the patient's brain was constructed. The electrode placement on the cortical surface was designed in Blender to cover the functional areas of the precentral and postcentral gyri. To import the positioning results into the surgical navigation system, we wrote the electrode locations into the patient's original T1 DICOM data. This process involved coordinate transformation between FreeSurfer's Surface RAS reference frame and the image's original RAS reference frame (Equation 1).

$$X' = AX \quad (1)$$

where X represents the homogeneous coordinates of the electrode points in the Surface RAS reference frame$(x, y, z, 1)$, X' represents the new coordinates in the original RAS reference frame (x', y', z'), and A is the transformation matrix (3×4) converting from the FreeSurfer's Surface RAS coordinate system to the DICOM image's scanner RAS coordinate system. An optimized kd-tree nearest neighbor algorithm was used to efficiently map these coordinates to the pixel points in the original DICOM images. In this setup, all pixels within a 1mm radius were marked with a value significantly higher than the maximum MRI intensity (e.g., 5000). The modified DICOM files were then imported into the navigation system, allowing the surgeon to directly determine the electrode positions during surgery. The final electrode implantation sites, as shown in Fig. 1d, matched the planned locations and the areas of optimal fMRI activation.

Impedance Measurement

The NEO system supports impedance measurement using milliampere (mA) stimulation current. The system uses a stimulation current of 1 mA with a pulse width of 1000 μs at a pulse frequency

of 10 Hz for a duration of 5000 ms. It measures the impedance between the epidural electrode contacts. Once a month, we record impedance data to track the trend of internal environment change (Fig. 2g).

Comparison of Three Types of Brain Electrophysiology Recordings

To compare the differences between epidural electrocorticography (eECoG) and subdural electrocorticography (sECoG), we utilized data from the publicly available Kai Miller dataset[10]. Since the motor imagery patterns of paralyzed patients are more similar to actual movements in healthy individuals[24], we selected real hand movement data from 10 patients whose electrodes covered the hand area. The cortical electrodes in the Kai Miller dataset had a spacing of 10 mm and a contact diameter of 2.3 mm. In our study, we used electrodes with a spacing of 8 mm and a contact diameter of 3.2 mm, which are comparable in size. The EEG electrode spacing in the patients' EEG caps was approximately 4 cm. To ensure consistent results, all three types of brain electrical activity were processed using the common average rereference method. Additionally, to study the spatial resolution differences between different brain recordings, we introduced motor imagery data from the BCI2000 dataset for comparison[11].

In terms of frequency, we calculated the Event-Related Spectral Perturbation (ERSP) for eECoG, sECoG, and EEG during the 0-2.5 seconds of movement relative to the 0-2.5 seconds of resting state (Equation 2). This allowed us to compare the modulation depths of different frequency bands across the different brain electrical activities.

$$ERSP = \frac{P_{task} - P_{rest}}{P_{rest}} \quad (2)$$

Where P_{task} refers to the power of the brain electrical activity in the frequency band during movement, and P_{rest} refers to the power in the resting state. Power spectral density (PSD) was calculated using resting state data to compare the spectral energy differences of the different brain electrical activities (Fig. 2b).

To qualitatively compare the spatial resolution differences, we calculated the relationship between the distance between electrode pairs and the correlation coefficient of the electrode signals (Fig. 2c). To maintain consistency with the number of subjects and tasks selected in the eECoG dataset, we selected all electrode pairs from the first 10 subjects in the BCI2000 dataset for real left- and right-hand movements. All eECoG signals were filtered with a 1 Hz high-pass filter, using the original reference electrodes (EEGs were referenced to mastoids, sECoGs and eECoGs were referenced to the scalp).

Spatio-Spectral Riemannian Geometry Decoding Method

The spatio-spectral information in eECoG signals can be described using a covariance matrix. Typical eECoG responses to motor imagery include ERSP across different frequency bands. By constructing a multi-band joint covariance matrix (Equation 3), we can effectively extract the spatio-spectral patterns of the EEG:

$$C_f = \begin{pmatrix} Z_{f_1} Z_{f_1}^T & \cdots & Z_{f_1} Z_{f_F}^T \\ \vdots & \ddots & \vdots \\ Z_{f_F} Z_{f_1}^T & \cdots & Z_{f_F} Z_{f_F}^T \end{pmatrix} \quad (3)$$

where $Z_{f_i}, i = 1, \ldots, F$ represents the channel signals filtered by different frequency bands, and F is the number of selected frequency bands.

The Affine Invariant Riemannian Metric (AIRM, Equation 4) can measure the distance between covariance matrices:

$$\delta_r(C_1, C_2) = \left\| C_1^{-\frac{1}{2}} C_2 C_1^{-\frac{1}{2}} \right\|_F = \left(\sum_{i=1}^{n} \log^2 \lambda_i \right)^{\frac{1}{2}} \quad (4)$$

where $\|\cdot\|_F$ represents the Frobenius norm, and λ_i are the eigenvalues of the matrix $C_1^{-1/2} C_2 C_1^{-1/2}$.

The AIRM metric has the following property: for any two samples from the source space that form covariance matrices S_A and S_B, mapping through a propagation matrix L (where L is invertible) results in sensor space covariance matrices $X_A = L S_A L^T$, $X_B = L S_B L^T$. It can be proven that:

$$\delta_r(X_A, X_B) = \delta_r(S_A, S_B)$$

This indicates that the separability in the source space and the sensor space is identical. Similarly, over long-term use, physiological changes may alter the propagation matrix L', but the AIRM distance measure ensures that separability remains unchanged. In contrast, BCI decoding algorithms using spatial filters may fail due to changes in the propagation matrix, causing spatial filter templates to become ineffective. Therefore, BCI decoding algorithms using the AIRM metric possess robustness in the sensor space and long-term stability.

To select the most effective frequency bands for decoding, we evaluated the separability of different frequency bands for resting and right-hand motor imagery states using a Riemannian-based class distinctiveness method.

Linear Discriminant Analysis (LDA) can be extended to construct class distinctiveness metrics under the Riemannian metric (Equation 5)[25]:

$$D(A, B) = \frac{\delta_r\left(\overline{C^A}, \overline{C^B}\right)}{\frac{1}{2}\left(\sigma_{C^A} + \sigma_{C^B}\right)} \quad (5)$$

where $\overline{C}$ represents the mean covariance under the Riemannian metric, and σ_C represents the standard deviation of the covariance under the Riemannian metric, $\sigma_C = \frac{1}{n-1}\sum_{i=1}^{n}\delta_r\left(C_i, \overline{C}\right)$. The superscripts $C^{(A/B)}$ indicate the corresponding classes.

Subsequently, a classifier based on AIRM can be constructed by embedding the data into the tangent space[26]. For the manifold M constituted by the aforementioned eECoG feature covariance matrices, the Fréchet mean point X_{ref} of the manifold can be found (Equation 6):

$$X_{ref} = \underset{X_{ref}}{\operatorname{argmin}} \sum_{i=1}^{N} \delta^2\left(X_i, X_{ref}\right) \quad (6)$$

Based on this point, the tangent space $T_{X_{ref}}M$ can be constructed, and the data points X_i can be embedded into this space to obtain the projected points S_i (Equation 7), where logm denotes the matrix logarithm operation.

$$S_i = \log_{X_{ref}}(X_i) = {X_{ref}}^{-\frac{1}{2}} \operatorname{logm}\left({X_{ref}}^{-\frac{1}{2}} X_i {X_{ref}}^{-\frac{1}{2}}\right) {X_{ref}}^{-\frac{1}{2}} \quad (7)$$

In our study, the epidural intracranial EEG of patients exhibits a typical Event Related Synchronization (ERS) effect at high frequencies (e.g., 55-95Hz) and a typical Event Related Desynchronization (ERD) effect at low frequencies (15-30Hz and 35-50Hz). Therefore, we designed a dual-frequency integrated spatio-spectral Riemannian geometry algorithm. Due to the physiological differences between low-frequency and high-frequency oscillatory activities, low-frequency activities were filtered at 15-30Hz and 35-50Hz, while high-frequency activities were band-pass filtered at 55-95Hz and then enveloped (Extended Data Fig. 3). Subsequently, a large covariance matrix of the feature signals was constructed, which was whitened to retain 99% of the variance dimension components to reduce the dimensionality. The samples were then embedded into the tangent space constituted by the Fréchet mean point, and finally sent to a logistic regression classifier to build the decoder for BCI calibration.

Control Decoding Methods

We employed two classical BCI decoding methods to evaluate our model. **Linear Model:** To evaluate the decoding method proposed in this paper, we selected a commonly used linear model as a baseline for comparison[1,27]. This linear model first uses a band-pass filter in the 0-150Hz frequency range to filter the signal into nine different frequency bands and then downsamples to 10Hz. The signals from the nine frequency bands and different channels are then concatenated into a 315-dimensional feature vector (7 channels * 9 frequency bands * 5 time points). Finally, this feature vector is used for decoding with a logistic regression classifier. We also used 10-fold cross-validation to optimize the regularization parameter of the logistic regression classifier to prevent overfitting. **Common Spatial Pattern (CSP) Model**: Additionally, since there is a close relationship between Riemannian methods and spatial filtering methods, we designed a model using CSP spatial filters to compare with the Riemannian method's results[13,28]. This model

constructs the covariance matrix using the same frequency bands as the Riemannian method. The CSP method is then used to calculate and retain 16 spatial filters. The energy features of the resulting 16-dimensional spatial patterns are used for decoding with a logistic regression classifier. For each model, 10-fold cross-validation is used to optimize the regularization parameter of the logistic regression classifier to prevent overfitting.

Decoding Continuous Grasping States using Hidden Markov Model

Considering that the natural grasping process is inherently continuous, with each state at a given time point being dependent on the preceding and following states, leveraging this dependency can significantly enhance the reliability of maintaining a grasp. The Hidden Markov Model (HMM), by constructing a multi-order stochastic process, links the probability of the current hidden state with the observed data and the probability of the hidden state at the previous time point. This can be used to describe the natural grasping process. We define the hidden states as either resting or grasping. In our constructed HMM algorithm, the emission probability $p(z_t|s_k)$ is derived from the Riemannian geometric classification model obtained through supervised training, while the transition probability matrix is semi-supervised, estimated using the forward-backward algorithm based on data from the patient's free-grasping training sessions. The first-order Hidden Markov Model can predict the probability of each hidden state at the current step based on the probability of each hidden state at the previous step (Equation 8):

$$p(s_{k,t}) = p(z_t|s_k)\sum_i p\left(s_{k,t}|s_{i,t-1}\right)p(s_{i,t-1}) \quad (8)$$

where z_t is the observed data at time t, and s_k is state k. We set a threshold p_{th}, and when the likelihood probability of the patient's new state exceeds this threshold, the model switches states. This threshold is estimated based on offline validation results and is set to 0.8 for the patient.

Additionally, we apply an extra step of first-order filtering to smooth the probabilities output by the HMM (Equation 9). The parameter η is adjusted based on offline validation results and is set to 0.7 for the patient.

$$\hat{p}_{curr} = \eta p_{last} + (1-\eta)p_{curr} \quad (9)$$

where p_{last} is the hidden state probability from the previous step, p_{curr} is the current hidden state probability inferred from Equation 6, and $\hat{p}_{curr}$ is the final estimated hidden state probability.

Brain-Computer Interface Training Paradigms

The calibration task is utilized for personalized model calibration and BCI testing. The paradigm consists of 15 trials per session, with each trial including 5 seconds of movement, feedback (10 seconds for success, 2 seconds for failure), and 5 seconds of resting state. The experiment begins with a 10-second period during which a crosshair appears at the center of the screen, and the participant needs to focus on the crosshair and remain calm. After 10 seconds, the actual task

begins. At the start of the motor imagery task, a one second blank screen is firstly given to remind the participant to prepare. After that, an arrow pointing left or right appears at the center of the screen, indicating left-hand or right-hand movement respectively, accompanied by a text prompt "Start imagining left-hand/right-hand movement." Feedback is provided after the motor phase, with the model making a judgment every second during the 5-second motor phase. The task has three difficulty levels: easy, medium, and hard, requiring correct judgments of 3, 4, and 5 times respectively. Only with correct judgments will the participant receive pneumatic hand feedback and a "Congratulations" message on the screen; otherwise, the message "Keep trying" will be displayed (Extended Data Fig. 5a). Before fixing the model, random feedback with an 85% accuracy rate is given. In the first session of the calibration paradigm, fake feedback is used. In the second calibration session, feedback results are calculated using the model calibrated with the first session of training data. After the second calibration session, the final model is trained using data from both sessions and fixed for the patient. We perform this calibration task monthly to periodically assess the model's performance.

During rehabilitation training, the patient uses the fixed model for free grasping tasks. The model makes a judgment every 0.1 seconds to determine the patient's grasping or relaxation state. To avoid false triggers caused by the EEG offset response after the patient’s releasing an object, there is a 3-second freeze period during which no new judgments are made. The model displays the confidence level of the grasp in the form of a progress bar on the screen, providing visual feedback to the participant. To quantitatively evaluate the effectiveness of the BCI system, we designed a **nine-square grid paradigm** requiring the patient to take objects to designated targets using the BCI. A 50.4 cm wide and 35.6 cm long nine-square grid board, as well as standard components of height 15 cm, upper cylinder diameter 4.5/6/6.5 cm, and lower disc diameter 10 cm were used in this paradigm (Extended Data Fig. 5b). The patient is instructed by the experimenter to use the BCI to drive the pneumatic hand to grasp the standard component from the center of the nine-square grid and move it to the designated color block position, then release the object by controlling the pneumatic hand. The test is repeated in two rounds, and the total time from the start of the instruction to the successful placement of the object is recorded to evaluate whether the patient can smoothly control the state switching of the BCI system. We also compared the patient's success rate with and without BCI assistance. Success is defined as completing the task within 10 seconds without touching the grid boundaries before picking up the object and without dropping it midway. Any other result is considered a failure.

Model Training and Evaluation

The model is trained based on two sets of calibration data. Since High Gamma (HG) activity decays over time during imagined grasping, we use data from the first 1.5 seconds after the onset of motor imagery and the entire 5 seconds of resting state as the training data. The data are segmented at 0.5-second intervals for model fitting. One set of data is used for model training, utilizing 10-fold cross-validation to select the optimal regularization parameters for the classifier. After fitting the classification model, we fit the HMM state transition matrix using the patient's grasping behavior data to construct a complete decoding model. Validation is conducted using a different set of data, evaluating both segment metrics and event metrics. After validation, a final model is trained using both sets of calibration data.

During model calibration, it is necessary to design evaluation criteria to assess the effectiveness of the model. Since the goal is to decode natural grasping states, which is a continuous time process, evaluation needs to consider both segment metrics (such as sample classification accuracy) and event metrics (sensitivity and specificity of event detection). **Segment Metrics**: The model directly classifies data segments and calculates classification accuracy. Additionally, due to the uneven distribution of classes in the segmented data samples, the F1 score (the harmonic mean of precision and recall) is used, which is insensitive to class imbalance. For segment metrics, the random level for the F1 score and AUC is 0.5. **Event Metrics**: To evaluate grasping accuracy over continuous time, we designed event-based metrics. If a grasping event is correctly identified within 0.5s before its onset and 2 seconds after it, it is considered a correct judgment; otherwise, it is a false negative. If more than one grasping event is detected during a single grasping event, it is considered a false positive. Precision, recall, and their harmonic mean (F1 score) are calculated accordingly. Due to the low frequency of grasping events, the random level for event metrics is low. Monte Carlo simulations estimate the random level for the F1 score of event metrics to be approximately 0.09 (with the grasping onset time covered about 10% of total time), indicating that continuous grasping tasks are relatively difficult, much harder than simple binary classification tasks.

Functional Rehabilitation Assessment Methods

This study uses the ISNCSCI scale and the ARAT scale to assess patients' neurological and upper limb functional status, respectively. The ISNCSCI scale is evaluated by two attending physicians, and any discrepancies in their evaluations are discussed to reach a single result. The ISNCSCI scale is measured monthly starting from the 2^{nd} to 9^{th} month post-surgery. The ARAT scale assessments are conducted by rehabilitation physicians and experimenters, with the process being video recorded.

The testing of somatosensory evoked potentials (SEP) follows the standards of the International Federation of Clinical Neurophysiology (IFCN)[29]. The stimulation sites are at the wrist corresponding to the median, radial and ulnar nerves respectively. A 6×9 cm silver/silver chloride adhesive electrode is used. The positive electrode is placed distally on the trunk, the negative electrode proximally, with a 2 cm distance between them. The stimulation is a unidirectional pulse, with 2 Hz frequency 400 μs pulse width and amplitudes of 16 mA for the median and radial nerves, or 12 mA for the ulnar nerve. This setup aims to stably evoke SEP while avoiding pain. The stimulation is repeated 160 times in each session. During stimulation, SEPs are recorded with epidural electrodes at a sampling rate of 1000 Hz. The signals are band-pass filtered (20-400 Hz) and averaged across trials to obtain the SEP waveform. Monthly recordings are repeated at the same stimulation site and parameters to observe changes in the SEP waveform.

In SEP analysis, for early (15-35 ms) and late (40-80 ms) SEP components, the average waveform amplitude is extracted. To minimize amplitude increases due to enhanced random phase oscillatory activity, the Bootstrap method is used. For each Bootstrap sample set, the average SEP response is extracted, and the average waveform amplitudes of early and late components are extracted. For the data from 1^{st} and 9^{th} month after implantation, permutation test is used to

calculate the p-values that 9th month's amplitude is greater than that of 1st month, and the FDR correction is applied to control the false discovery rate in multiple comparisons.

Hand Trajectory Recognition in the Free Grasping paradigms

To accurately capture hand movement trajectories during the free grasping process, a USB webcam was positioned directly above the experimental table to record the hand movements from a top-down perspective (Extended Data Fig. 9). A serial port synchronization signal and LED light were used to synchronize the video recording with the EEG data. For the video data of both pneumatic hand grasping and bare hand grasping, we finetuned a hand keypoint detection model to analyze the hand movement trajectories. The main structure of the model utilizes a high-resolution convolutional network (HRNet)[30] pre-trained on the OneHand10k dataset. The detection algorithm employs distribution-aware coordinate representation (DARK)[31] based on heatmaps to detect four key points of the pneumatic hand or the hand: the index fingertip, thumb tip, the base of the thumb (thenar), and the wrist. For the patient's grasping data, the coordinates of the thenar key point were extracted as the hand movement trajectory. The start time of each trial was defined as the moment the hand contacted the central cylindrical object, and the end time was defined as the moment of grasping failure or successfully reaching the target position and releasing the object. The model was fine-tuned based on the OneHand10K pre-trained model. The pneumatic hand model training data included 1,295 annotated images with a resolution of 960x540, with 80% of the data used for training and 20% for testing. The keypoint recognition model achieved an AUC of 0.89. The bare hand detection model training data included 1,118 annotated images with a resolution of 960x540, with 80% of the data used for training and 20% for testing. The model achieved an AUC of 0.85.

Acknowledgement

We thank our volunteer and his family for their commitment and trust. We thank Sichang Chen and Lin Liu from Xuanwu Hospital of Capital Medical University, Yujing Wang and Xiaoshan Huang from Neuracle Technology Co., Zheng Yan from Huaqiao University, Ze'ao Xiong, Ruwei Yao, Yunjing Li, Le Yu, Yichao Li from Tsinghua University, and Zhouxingyu Yan from John Hopkins University for their help in this work.

Reference

1. Benabid, A. L. *et al.* An exoskeleton controlled by an epidural wireless brain–machine interface in a tetraplegic patient: a proof-of-concept demonstration. *Lancet Neurol.* **18**, 1112–1122 (2019).
2. Moses, D. A. *et al.* Neuroprosthesis for Decoding Speech in a Paralyzed Person with Anarthria. *N. Engl. J. Med.* **385**, 217–227 (2021).
3. Lorach, H. *et al.* Walking naturally after spinal cord injury using a brain–spine interface. *Nature* **618**, 126–133 (2023).
4. Samejima, S. *et al.* Brain-computer-spinal interface restores upper limb function after spinal cord injury. *IEEE Trans. Neural Syst. Rehabil. Eng.* **29**, 1233–1242 (2021).
5. Patel, P. R. *et al.* Utah array characterization and histological analysis of a multi-year implant

in non-human primate motor and sensory cortices. *J. Neural Eng.* **20**, (2023).

6. Branco, M. P., Geukes, S. H., Aarnoutse, E. J., Ramsey, N. F. & Vansteensel, M. J. Nine decades of electrocorticography: A comparison between epidural and subdural recordings. *Eur. J. Neurosci.* **57**, 1260–1288 (2023).
7. Anderson, M. A. *et al.* Natural and targeted circuit reorganization after spinal cord injury. *Nat. Neurosci.* **25**, 1584–1596 (2022).
8. Zeng, F.-G., Rebscher, S., Harrison, W., Sun, X. & Feng, H. Cochlear Implants: System Design, Integration, and Evaluation. *IEEE Rev. Biomed. Eng.* **1**, 115–142 (2008).
9. Formento, E. *et al.* Electrical spinal cord stimulation must preserve proprioception to enable locomotion in humans with spinal cord injury. *Nat. Neurosci.* **21**, 1728–1741 (2018).
10. Miller, K. J. A library of human electrocorticographic data and analyses. *Nat. Hum. Behav.* **3**, 1225–1235 (2019).
11. Schalk, G., McFarland, D. J., Hinterberger, T., Birbaumer, N. & Wolpaw, J. R. BCI2000: A General-Purpose Brain-Computer Interface (BCI) System. *IEEE Trans. Biomed. Eng.* **51**, 1034–1043 (2004).
12. Congedo, M., Barachant, A. & Bhatia, R. Riemannian geometry for EEG-based brain-computer interfaces; a primer and a review. *Brain-Computer Interfaces* **4**, 155–174 (2017).
13. Koles, Z. J. The quantitative extraction and topographic mapping of the abnormal components in the clinical EEG. *Electroencephalogr. Clin. Neurophysiol.* **79**, 440–447 (1991).
14. Inanici, F., Brighton, L. N., Samejima, S., Hofstetter, C. P. & Moritz, C. T. Transcutaneous Spinal Cord Stimulation Restores Hand and Arm Function after Spinal Cord Injury. *IEEE Trans. Neural Syst. Rehabil. Eng.* **29**, 310–319 (2021).
15. Moritz, C. *et al.* Non-invasive spinal cord electrical stimulation for arm and hand function in chronic tetraplegia : a safety and efficacy trial. *Nat. Med.* **30**, 18–24 (2024).
16. Kramer, J. K., Taylor, P., Steeves, J. D. & Curt, A. Dermatomal somatosensory evoked potentials and electrical perception thresholds during recovery from cervical spinal cord injury. *Neurorehabil. Neural Repair* **24**, 309–317 (2010).
17. Kramer, J. L. K., Moss, A. J., Taylor, P. & Curt, A. Assessment of posterior spinal cord function with electrical perception threshold in spinal cord injury. *J. Neurotrauma* **25**, 1019–1026 (2008).
18. Yozbatiran, N., Der-Yeghiaian, L. & Cramer, S. C. A standardized approach to performing the action research arm test. *Neurorehabil. Neural Repair* **22**, 78–90 (2008).
19. Luo, S. *et al.* Stable Decoding from a Speech BCI Enables Control for an Individual with ALS without Recalibration for 3 Months. *Adv. Sci.* **10**, 1–12 (2023).
20. Milekovic, T. *et al.* Stable long-term BCI-enabled communication in ALS and locked-in syndrome using LFP signals. *J. Neurophysiol.* **120**, 343–360 (2018).
21. Fountas, K. N. & Smith, J. R. Subdural electrode-associated complications: A 20-year experience. *Stereotact. Funct. Neurosurg.* **85**, 264–272 (2007).
22. Donati, A. R. C. *et al.* Long-Term Training with a Brain-Machine Interface-Based Gait Protocol Induces Partial Neurological Recovery in Paraplegic Patients. *Sci. Rep.* **6**, 1–16 (2016).
23. Jovanovic, L. I. *et al.* Restoration of Upper Limb Function after Chronic Severe Hemiplegia: A Case Report on the Feasibility of a Brain-Computer Interface-Triggered Functional Electrical Stimulation Therapy. *Am. J. Phys. Med. Rehabil.* **99**, e35–e40 (2020).

24. Lotze, M. & Halsband, U. Motor imagery. *J. Physiol. Paris* **99**, 386–395 (2006).
25. Yamamoto, M. S., Lotte, F., Yger, F. & Chevallier, S. Class-distinctiveness-based frequency band selection on the Riemannian manifold for oscillatory activity-based BCIs: preliminary results. in *2022 44th Annual International Conference of the IEEE Engineering in Medicine & Biology Society (EMBC)* vols 2022-July 3690–3693 (IEEE, 2022).
26. Barachant, A., Bonnet, S., Congedo, M. & Jutten, C. Classification of covariance matrices using a Riemannian-based kernel for BCI applications. *Neurocomputing* **112**, 172–178 (2013).
27. Moly, A. *et al.* An adaptive closed-loop ECoG decoder for long-term and stable bimanual control of an exoskeleton by a tetraplegic. *J. Neural Eng.* **19**, (2022).
28. Lemm, S., Blankertz, B., Curio, G. & Müller, K. R. Spatio-spectral filters for improving the classification of single trial EEG. *IEEE Trans. Biomed. Eng.* **52**, 1541–1548 (2005).
29. Cruccu, G. *et al.* Recommendations for the clinical use of somatosensory-evoked potentials. *Clin. Neurophysiol.* **119**, 1705–1719 (2008).
30. Wang, J. *et al.* Deep High-Resolution Representation Learning for Visual Recognition. *IEEE Trans. Pattern Anal. Mach. Intell.* **43**, 3349–3364 (2021).
31. Zhang, F., Zhu, X., Dai, H., Ye, M. & Zhu, C. Distribution-Aware Coordinate Representation for Human Pose Estimation. *Proc. IEEE Comput. Soc. Conf. Comput. Vis. Pattern Recognit.* 7091–7100 (2020) doi:10.1109/CVPR42600.2020.00712.

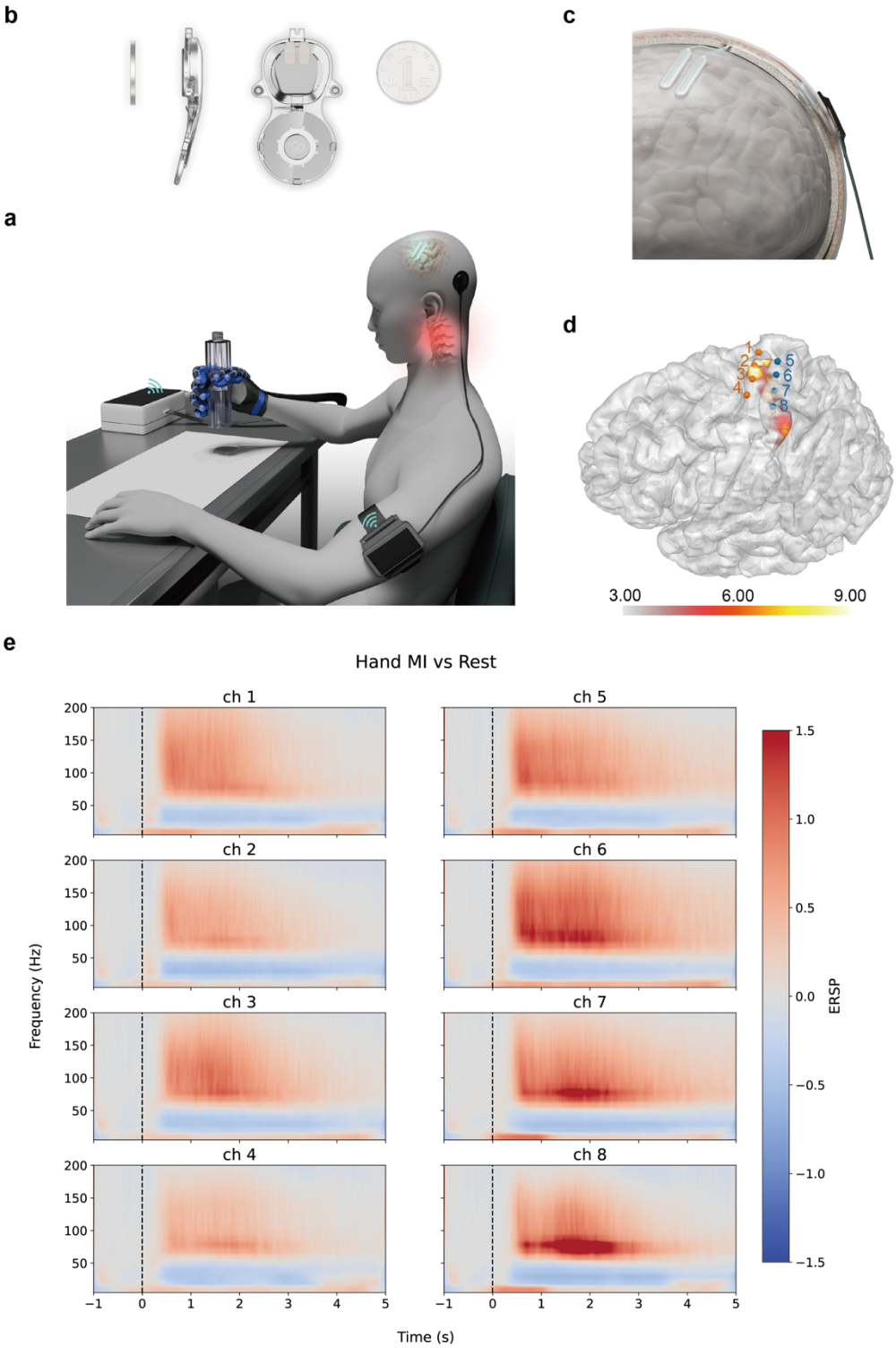

Figure 1 NEO system design and basic signal characteristics. a, Diagram of the NEO brain-computer interface (BCI) system. The NEO BCI system transmits epidural ECoG through a coil to an external device fixed on the patient's shoulder. The external device sends the signals to the host computer, where an algorithm decodes the patient's grasping intention and drives a pneumatic glove to grasp objects. When the patient stops imagining the grasp, the pneumatic glove is driven to open and release the object. b, Structure of the NEO implant. The upper part is the implant, and the lower part is the coil. c, Diagram of the NEO implant implantation position. The coil is magnetically attached through the skin,

transmitting signals and power. Electrodes are fixed on the surface of the dura mater and connected to the implant through a skull tunnel. d, Diagram of the patient implantation position. The orange and blue dots represent the electrodes on the precentral and postcentral gyrus, respectively. The heat map overlaying the cortex represents functional MRI activation significance values (negative logarithm of p values). e, Event-related spectral perturbation (ERSP) during imagined grasping. The spectral pattern exhibits a typical dual-frequency characteristic, including low-frequency (15-50 Hz) ERD and high-frequency (>50 Hz) ERS. Hand-MI: Hand Motor Imagery.

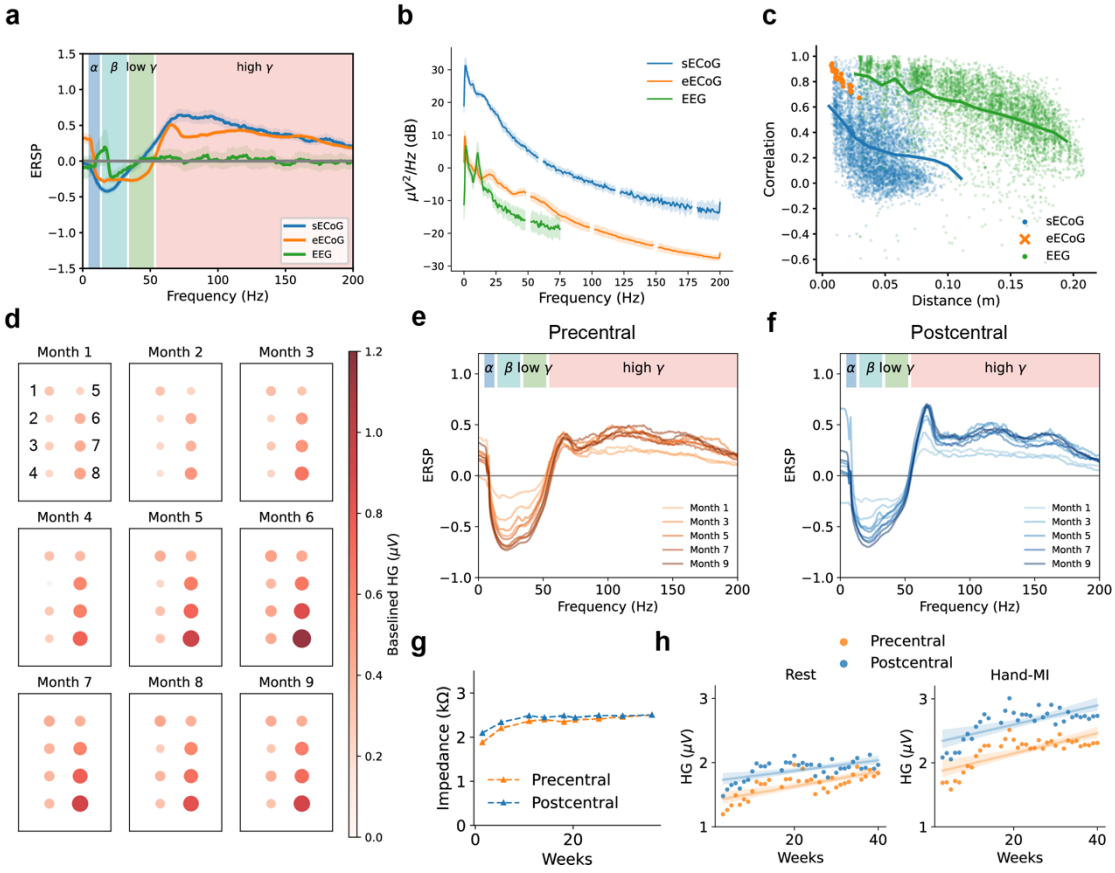

Figure 2 Long-term spatio-temporal-spectral characteristics of epidural signals. a, Comparison of event-related spectral perturbations (ERSP) among subdural ECoG, epidural ECoG, and scalp EEG. Epidural ECoG exhibits an effective frequency band range similar to subdural ECoG. b, Comparison of PSD among the three types of electrophysiological recordings. Subdural ECoG has the highest amplitude, and epidural ECoG has a higher amplitude in the higher frequency band (30-70 Hz) compared to scalp EEG. The PSD excludes the frequency band of power line interference. c, Relationship between channel signal correlation and electrode distance. d, Trend of high-frequency energy (55-95 Hz) spatial patterns of epidural ECoG during imagined hand movements. Long-term training significantly enhances high-frequency activity in the ECoGs of all channels during motor imagery (Month 1 vs. Month 6, $p<0.001$). Channels where the HG response is not significantly greater than zero are marked as gray. e-f, Trend of the average ERSP of precentral and postcentral electrodes, with each curve representing the average ERSP of one month's hand motor imagery data. Both low-frequency ERD and high-frequency ERS gradually increase with training. g, Impedance changes of precentral and postcentral electrodes. h, Trend in high-frequency energy (55-95 Hz, un-baselined) of precentral and postcentral electrodes during rest and hand motor imagery, both showing significant positive correlations ($p<0.001$). In a, b, and c, subdural ECoG data are from the Kai Miller dataset[10]; a and b use scalp EEG from the patient's own recordings;

c uses scalp EEG from the BCI2000 dataset[11]. Hand-MI: Hand Motor Imagery. HG: High-Gamma band power.

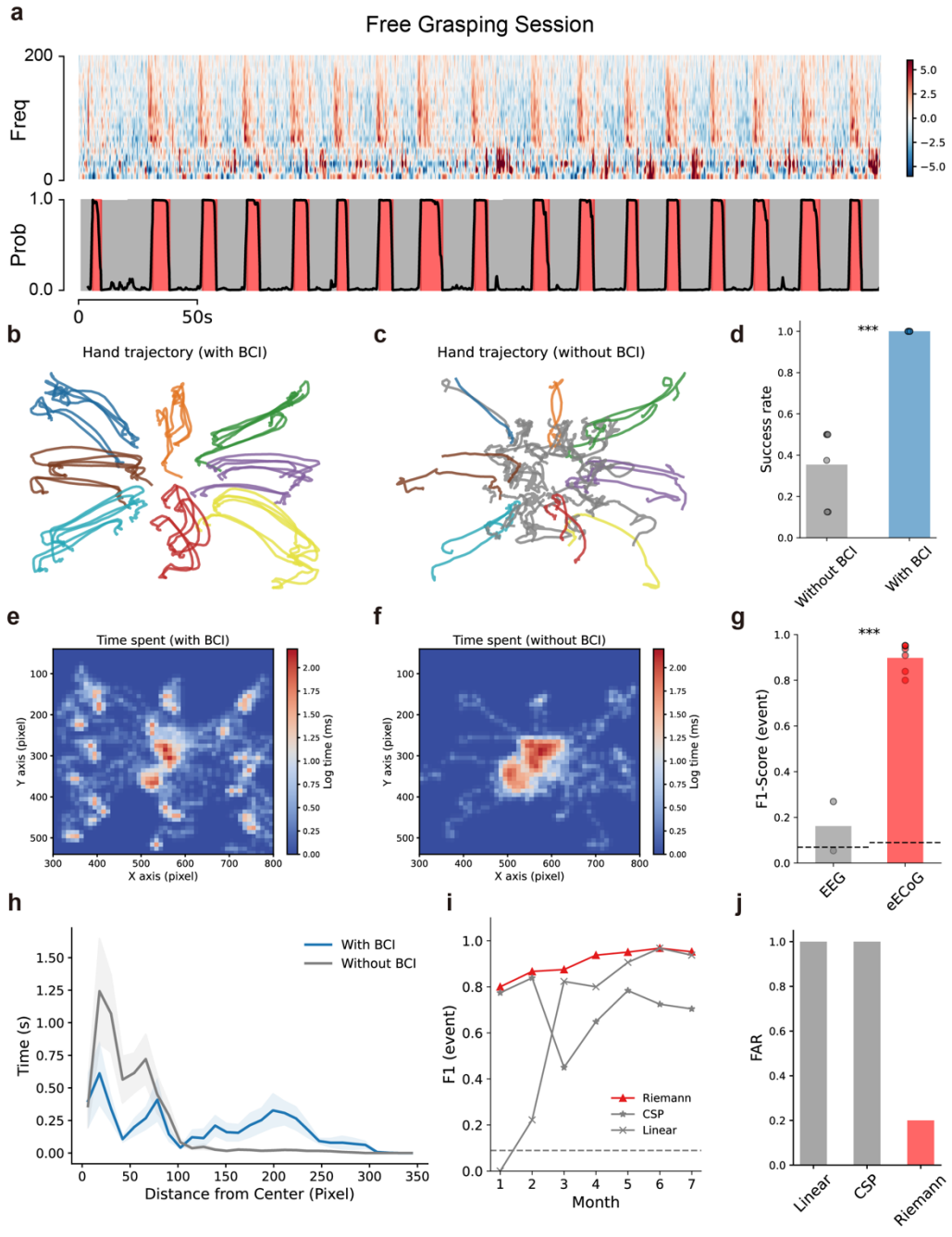

Figure 3 Minimally invasive epidural brain-computer interface (BCI) for motor assistance. a, Example of BCI testing data and decoded confidences. The red shading indicates the time range of the grasping action as determined by the decoder. The grasping action has a high single-trial signal-to-noise ratio. b-c, Hand movement trajectories of the patient performing the BCI testing task with BCI assistance (b) or unaided (c), recorded by a top-down camera and identified by a keypoint detection model. d, With BCI assistance, the patient's success rate of moving the object to the designated position within 10 seconds is 100%, whereas, without BCI assistance, the success rate is only 35%. e-f, Logarithmic spatial distribution of the time spent with BCI assistance (e) or unaided (f). With BCI assistance, the time spent

is clustered in the target start and end points, while unaided, the time was mostly spent in the start area. g, Comparison of F1 scores for detecting grasping events using epidural ECoG and scalp EEG. The black dashed line represents the chance level. Epidural ECoG detection F1 scores are significantly higher than those of scalp EEG. h, Distribution of the relationship between time spent and distance to the central start point. With BCI assistance, the patient can pick up the object and move to the edge more quickly. i, Changes in the F1 score of the decoding algorithm for detecting grasping events over 7 months. The Riemannian geometry-based decoding method shows long-term stability, outperforming the control linear method and CSP method. The gray dashed line represents the chance level. j, Robustness of different models to electromyographic (EMG) noise generated by chewing during daily use. Due to its high specificity to spatial patterns, the Riemannian geometry method shows greater robustness to EMG noise from chewing, which has a different spatial pattern from grasping, compared to the linear method and the CSP method. FAR: False Activation Rate.

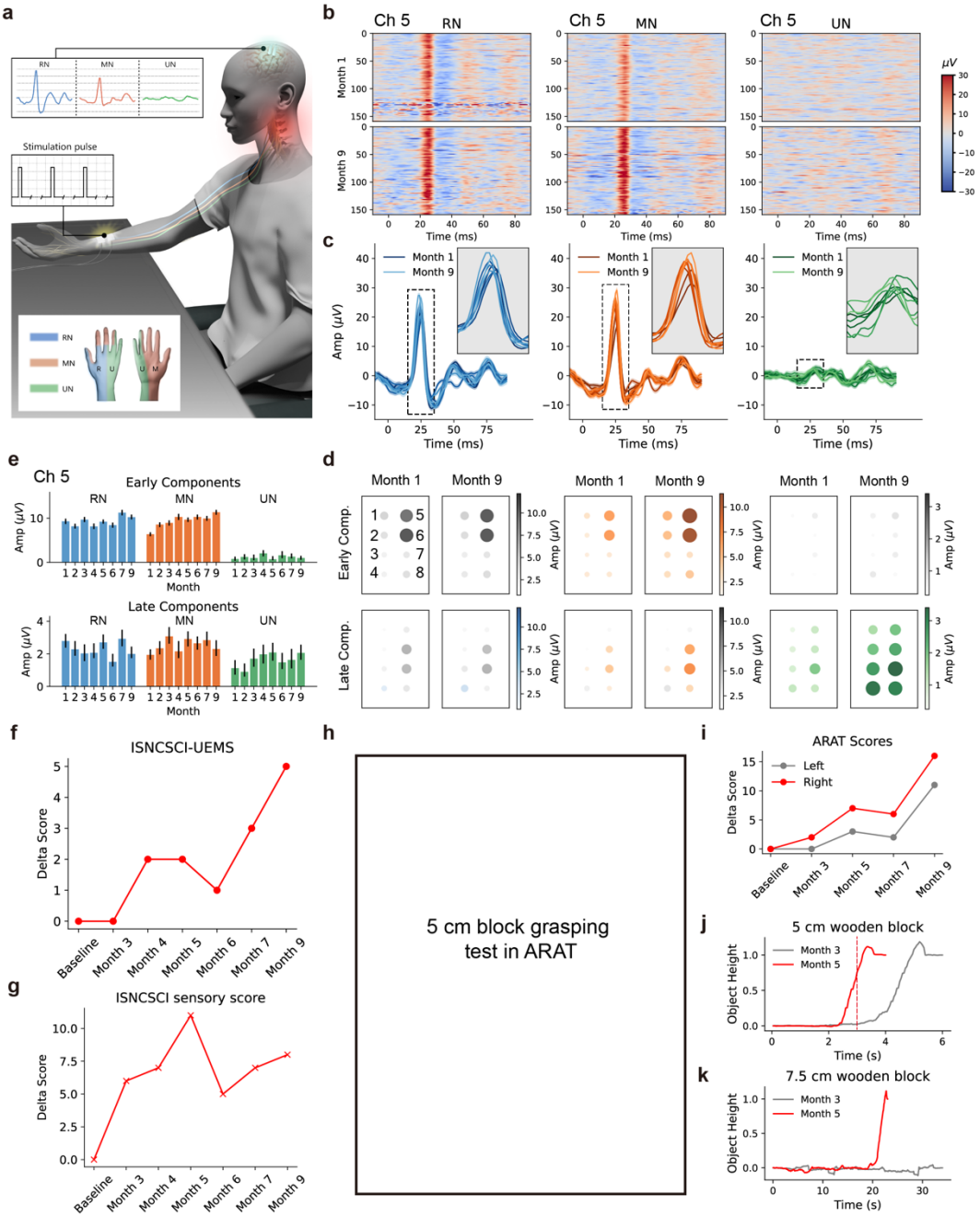

Figure 4 Electrophysiological and functional rehabilitation assessments. a, Diagram of sensory evoked potential (SEP) measurement. Functional stimulators were used to stimulate the patient's radial, median, and ulnar nerves, and SEP activities were recorded from NEO epidural electrodes. b, Trial images of SEP waveforms (channel 5) for the patient's radial nerve (left), median nerve (center), and ulnar nerve (right) at the 1st and 9th months. c, SEP waveforms over 9 months, with colors from dark to light representing SEP waveforms over the 9 months (channel 5). d, Changes in average amplitude of early SEP components (15-35 ms) and late SEP components (40-80 ms) at different electrodes from the 1st month to the 9th month. Electrodes with no significant enhancement ($p>0.05$, FDR-corrected) were marked in gray. e, Relationship of average amplitude changes over time for early SEP components (15-35 ms, top) and late SEP components (40-80 ms, bottom) of channel 5. f, Changes in key muscle strength in the upper limbs according to the ISNCSCI scale. g, Changes in sensory scores of the ISNCSCI scale. Sensory

scores encountered a considerable decrease in the 6th month due to the patient's use of antispasmodic medication. h, The patient grasping and releasing a 5 cm block in the Action Research Arm Test (ARAT) test at the 3rd and 5th months. The red curve represents the block trajectory, the boxes mark the start and end points, and the dashed lines indicate the height of the lift. i, Changes in ARAT scores over the course of training, with the right hand showing greater improvement than the left hand. j-k, Changes in lift height of 5 cm and 7.5 cm blocks over time during grasp and release tasks in the ARAT test at the 3rd and 5th months, with the red dashed line indicating the time point shown in h. Trajectories were obtained from video recordings and manually annotated. MN: median nerve; RN: radial nerve; UN: ulnar nerve.

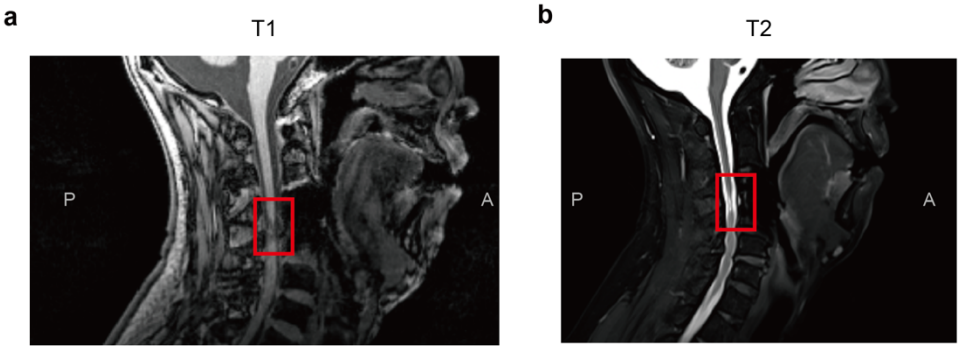

Extended Data Figure 1 MRI Scans of the Patient's Head and Neck (A) Cervical spine T1 structural image (B) Cervical spine T2 structural image; the red box indicates the location of the patient's spinal cord injury.

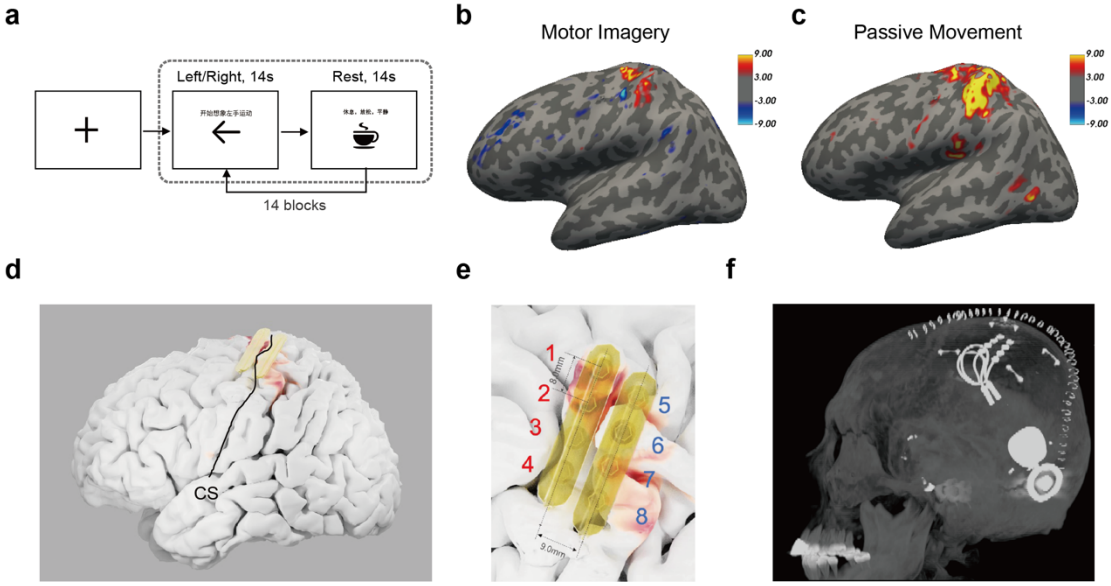

Extended Data Figure 2 fMRI Localization Paradigm and Surgical Planning. a, fMRI functional localization paradigm, including alternating rest and movement states of the left or right hand. b-c, Functional activation during motor imagery (b) and passive movement (c), with activation values represented as -lg(p). d, Electrode planning. e, Enlarged view of the diagram of the planned electrodes. Electrodes 1-4 were located on the precentral gyrus and electrodes 5-8 on the postcentral gyrus. f, Sagittal View of postoperative CT, showing the actual implantation positions. CS: Central Sulcus.

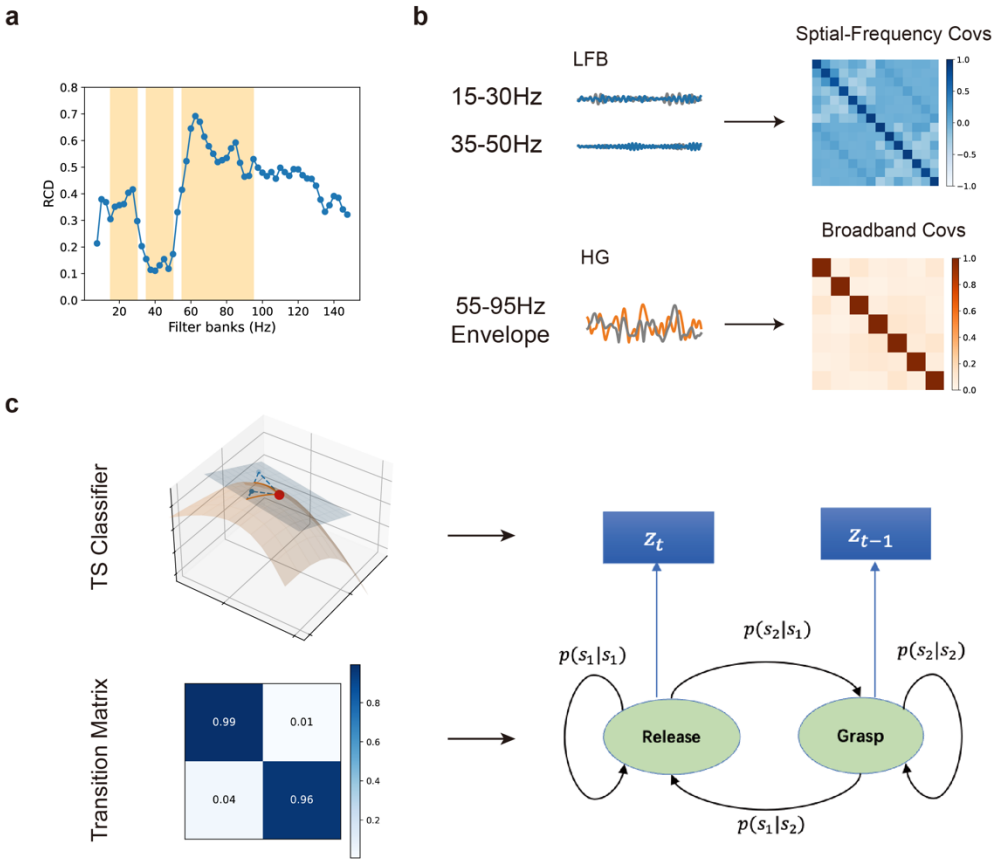

Extended Data Figure 3 Brain-Computer Interface Decoding Methods. a, Band selection using Riemannian class distinctiveness (RCD) across different frequency bands. b, Construction of the covariance feature matrix using low-frequency band-pass filter features and high-frequency envelope features. c, Decoding framework for natural grasping based on the Hidden Markov Model (HMM), utilizing the temporal dependence of grasp states to ensure the reliability of continuous grasping. The observation model is based on the trained Riemannian geometry classifier, and the transition matrix is fitted based on patient behavior data. TS Classifier: Tangent Space Classifier.

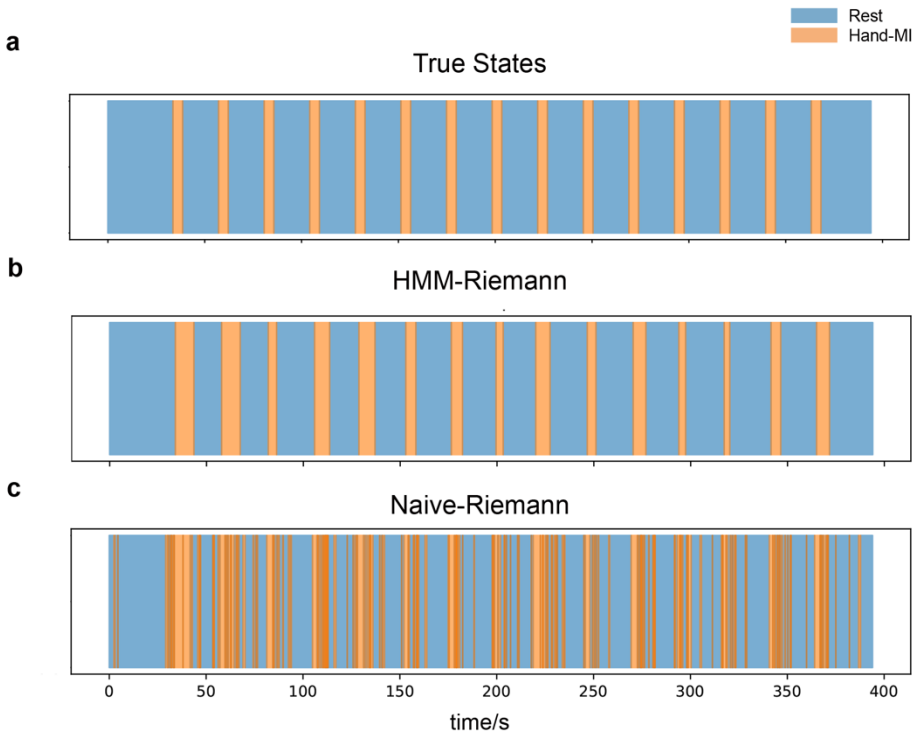

Extended Data Figure 4 Illustration of HMM decoding. a, Actual motor imagery cues. b, Continuous grasping decoded by the HMM-Riemann method. c, Continuous grasping decoded by the Naïve-Riemann method without HMM. Hand-MI: Hand Motor Imagery.

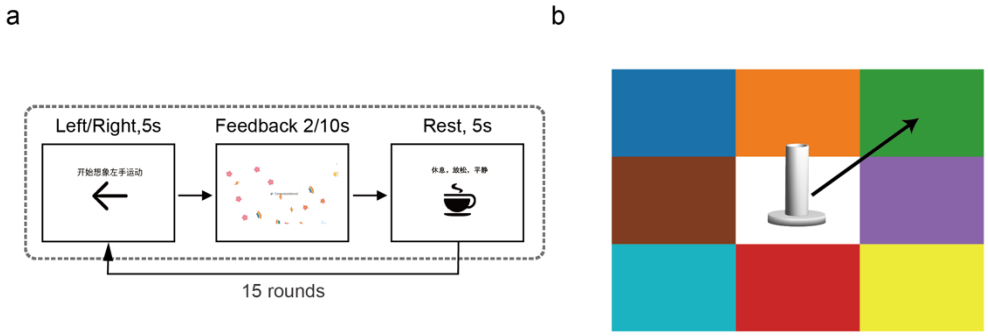

Extended Data Figure 5 Calibration and Training Paradigms. a, BCI calibration paradigm. b, Free grasp BCI testing paradigm, where the patient needs to move the standard cylinder from the center to the grid designated by the experimenter.

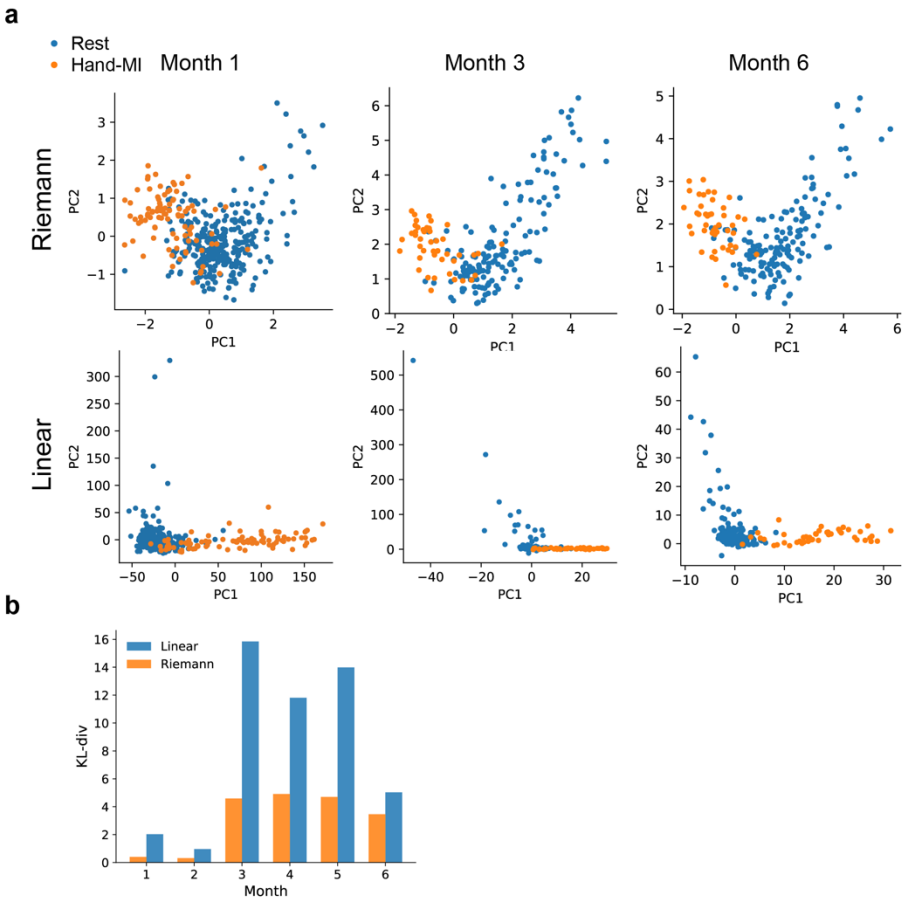

Extended Data Figure 6 Changes in epidural ECoG Feature Distribution During Long-term Use. a, Scatter plots of PCA-embedded distributions of Riemannian features and linear spatio-temporal-spectral features across different months. b, Changes in KL divergence between Riemannian features and linear spatio-temporal-spectral features compared to training data over different months. The stability of Riemannian features consistently surpasses that of linear spatio-temporal-spectral features. Hand-MI: Hand Motor Imagery. KL-div: KL Divergence.

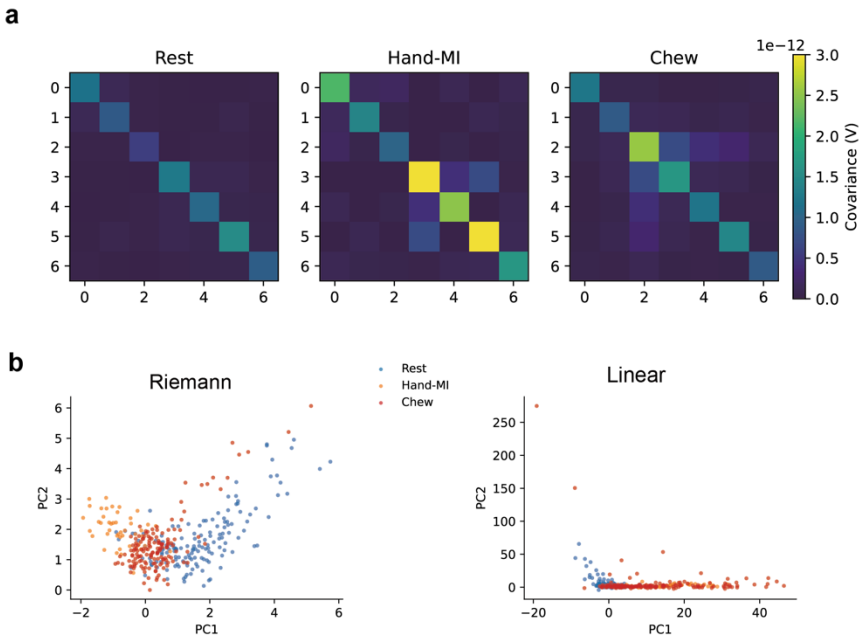

Extended Data Figure 7 EMG Noise Pattern. a, Average covariance patterns of resting, motor imagery (Hand-MI), and EMG noise. b, Dimensionality-reduced spatial distribution patterns of Riemannian embedded features (left) and linear spatio-temporal-spectral features (right). Under Riemannian metrics, chewing EMG noise is positioned between resting and hand motor imagery; in linear spatio-temporal-spectral features, chewing noise highly overlaps with hand motor imagery distribution.

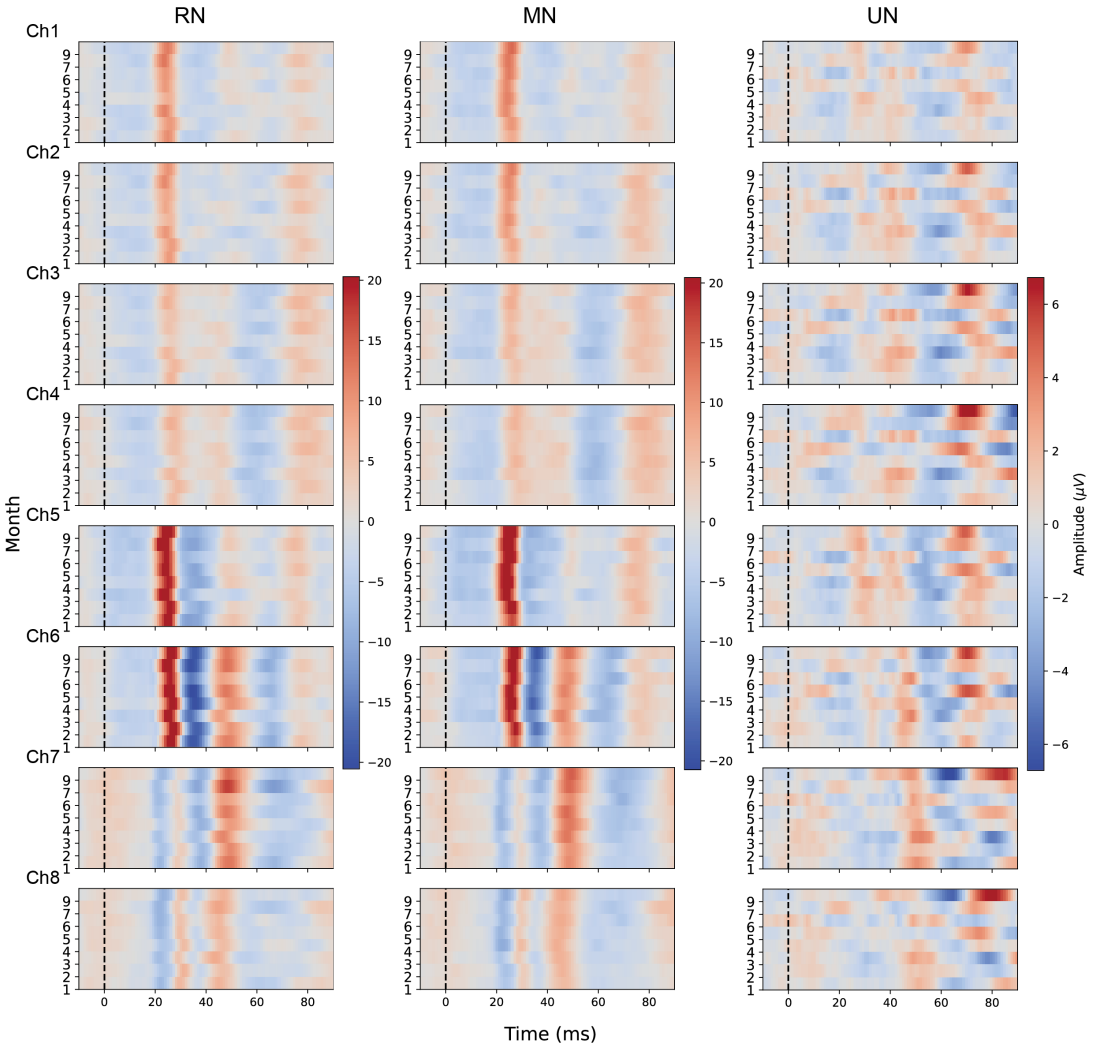

Extended Data Figure 8 Average Somatosensory Evoked Potential (SEP) Waveforms for Each Nerve, Channel, and Month. From top to bottom: Ch1-Ch8.

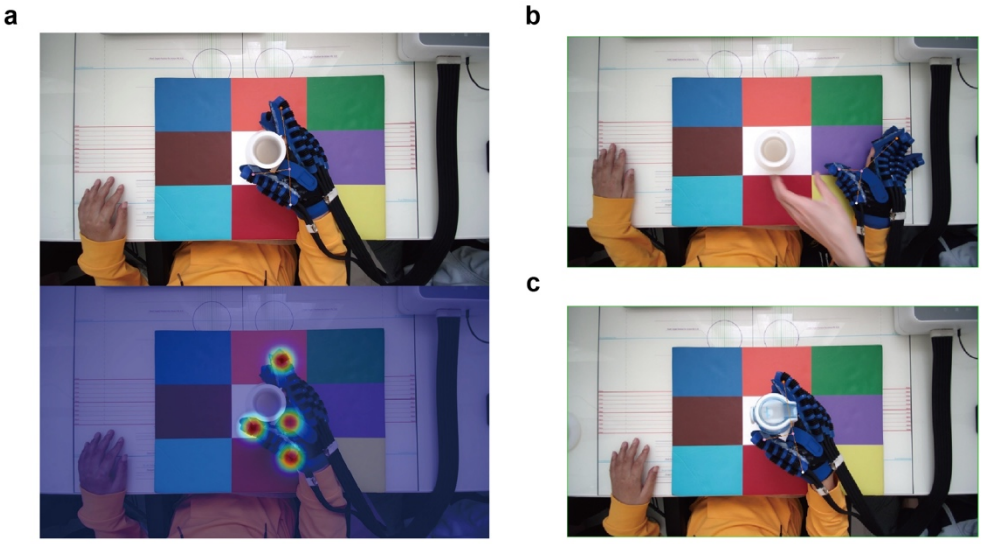

Extended Data Figure 9 Pneumatic Hand Keypoint Detection Model. a, Example of a detection heatmap. b-c, Examples of detection results.

839

Time	Pre-Operation	Month 3	Month 4	Month 5	Month 6	Month 7	Month 9
American Spinal Injury Association Impairment Scale (AIS)	A	A	A	A	A	A	A
Neurological level of injury	C4	C4	C4	C4	C4	C4	C4
Upper Extremity Motor Score							
C5, (Left | Right)	4 | 4	4 | 4	4 | **5**	4 | 5	4 | 5	4 | 5	**5** | 5
C6, (Left | Right)	3 | 3	3 | 3	3 | 3	3 | **4**	3 | **3**	3 | 3	3 | **4**
C7, (Left | Right)	2 | 2	2 | 2	2 | **3**	2 | **2**	2 | **2**	2 | **3**	2 | 3
C8, (Left | Right)	0 | 0	0 | 0	0 | 0	0 | 0	0 | 0	**1** | 0	**0** | **1**
T1, (Left | Right)	0 | 0	0 | 0	0 | 0	0 | 0	0 | 0	0 | 0	0 | 0
Total, (Left | Right)	9 | 9	9 | 9	9 | 11	9 | 11	9 | 10	10 | 11	10 | 13
Light Touch Sensory Score Total, (Left | Right)	7 | 8	9 | 7	8 | 9	11 | 9	7 | 7	7|7	7|7
Pin Prick Sensory Score Total, (Left | Right)	6 | 7	10 | 8	10 | 8	11 | 8	10 | 9	11|10	11|11
Deep Anal Pressure	No	No	No	No	No	No	No
Voluntary Anal Contraction	No	No	No	No	No	No	No

840 Extended Data Table 1 ISNCSCI Scores

841

842

	RN		MN		UN	
	Early	Late	Early	Late	Early	Late
Ch1	0.2461	0.0901	<0.0001	0.0746	0.1579	0.0069
Ch2	0.2369	0.2654	<0.0001	0.1905	0.3035	0.0007
Ch3	0.2555	0.0479	0.0235	0.0119	0.2198	<0.0001
Ch4	0.1068	0.0021	0.0396	0.0381	0.1161	<0.0001
Ch5	0.0078	0.9957	<0.0001	0.1021	0.2586	0.0013
Ch6	0.5814	0.9572	<0.0001	<0.0001	0.1724	<0.0001
Ch7	0.3704	0.184	0.0176	<0.0001	0.3169	0.0001
Ch8	0.3518	0.9889	<0.0001	0.0001	0.2373	<0.0001

843 Extended Data Table 2 p-values for Increases in Average Amplitudes of Early and Late SEP
844 Components for Different Nerves from Month 1 to Month 9 with Electrical Stimulation.

845

846

	Baseline		**Month 3**		**Month 5**		**Month 7**		**Month 9**	
	L	**R**	**L**	**R**	**L**	**R**	**L**	**R**	**L**	**R**
Grasp (18)	6	4	5	6	6	10	6	9	12	13

Grip (12)	6	6	6	6	6	6	6	6	7	10
Pinch (18)	2	2	2	2	4	4	3	4	5	6
Gross (9)	7	9	8	9	8	8	8	8	8	8
Total (57)	21	21	21	23	24	28	23	27	32	37

Extended Data Table 3 ARAT scores

Extended Data Video 1 NEO System Overview.

This video outlines the basic setup of the NEO brain-computer interface (BCI) system. First, the NEO implant is powered on. Next, the pneumatic hand is attached and configured. Once connected to the controller, the NEO system transmits epidural ECoG signals in real-time. Finally, the subject is able to control the pneumatic hand using his thoughts. Link to view online:
https://cloud.tsinghua.edu.cn/f/af0fb0644b43496fa4e7/

Extended Data Video 2 ARAT Grasping Test.

This video demonstrates the subject's improvement in hand function following a 9-month training period. It compares the subject's performance on ARAT tasks before surgery (baseline) and at the 9-month mark for both hands. For the right hand, grasping tasks involving 2.5 cm, 5 cm, and 7.5 cm cubes, as well as a 7.5 cm sphere, are compared between the baseline and 9th month. For the left hand, the grasping task with a sharpening stone is evaluated. Link to view online:
https://cloud.tsinghua.edu.cn/f/958b6cad79dd42c4ad12/

Extended Data Video 3 NEO for Hand Function Assistance.

This video demonstrates how the NEO system assists in hand function. With the help of the BCI system, the subject successfully lifts a bottle of water and moves it to the designated target area. Link to view online:
https://cloud.tsinghua.edu.cn/f/e8661aa219b14a988a43/

Extended Data Video 4 NEO for Independent Home Use.

This video highlights how the NEO system enhances the subject's daily life. Using the NEO system, the subject can independently eat with a customized fork and drink from either a plastic bottle or glass. Link to view online:
https://cloud.tsinghua.edu.cn/f/836149c8500441c3abd8/